JOURNAL OF SPACECRAFT AND ROCKETS
Vol. 35, No. 2, March–April 1998

Spacecraft Plasma Environment and Contamination Simulation Code: Description and First Tests

Jean-François Roussel*
ONERA, 31055 Toulouse, France

A new code devoted to spacecraft local induced environment simulation is presented. Its general frame, spacecraft geometry and mesh, and plasma module are described. The three-dimensional mesh, although of a structured rectangular type, allows a good representation of spacecraft surface positions and orientations due to the automatic generation of partial cubes by an object description language. The particle-in-cell plasma module can simulate time evolution and was stable for cell-size-to-Debye-length ratios as large as 60. The main contributions of this study are four test simulations. The first three, Child–Langmuir law and two Langmuir probes, are borrowed from plasma physics, and their solutions are known, either analytically or numerically. They constitute extensive testing of the plasma code over a wide range of Debye lengths. The last simulation, a typical low-Earth-orbit environment, was more complex, and only partial validation was achieved.

Nomenclature

$\boldsymbol{B}$ = magnetic field
$\boldsymbol{E}$ = electric field
E_n = normal electric field at mesh boundary
e = elementary electric charge, $+1.6 \times 10^{-19}$ C
$f_{i,e,s}$ = ionic/electronic distribution function in phase space (function of $\boldsymbol{x}$, $\boldsymbol{v}$, t)
$I_{i,e}$ = ionic/electronic collected current
J_{CL} = Child–Langmuir space charge limited current
k = Boltzmann constant
L = distance between injection and collection planes (Child–Langmuir one dimensional)
$m_{i,e,s}$ = particle mass
$n(x)$ = local particle density
n_0 = reference density (at infinity for Boltzmann equation)
$q_{i,e,s}$ = particle charge
S = probe surface, 1.37 cm^2 for the cylindrical probe
$T_{i,e,s}$ = ionic/electronic temperature
t = time
$\boldsymbol{v}$ = velocity vector
$\boldsymbol{x}$ = position vector
x = distance from injection plane (Child–Langmuir one dimensional)
α_{DN} = coefficient for mixed Dirichlet–Neumann boundary conditions
ε_0 = vacuum electrical permittivity
$\rho_{i,e,s}(\boldsymbol{x})$ = ionic/electronic local charge density
χ = probe electric potential
$\chi(\boldsymbol{x}), \chi(x)$ = local electric potential
χ_b = electric potential at mesh boundary
χ_0 = potential of the biased plane (Child–Langmuir one dimensional), -35 V

Subscripts

e = electronic
i = ionic
s = generic, either i or e

Introduction

UNDERSTANDING the interaction of the space environment involves two different aspects: knowledge of the undisturbed space environment and the evaluation of its effects on spacecraft subsystems. The presence of the spacecraft does not significantly alter some components of the space environment, such as ionizing radiations, micrometeoroids, atomic oxygen (ATOX) fluxes, uv fluxes, etc. Other components, however, have a locally induced environment that is drastically different from the undisturbed one. Such is the case for the local molecular and (cold) plasma environments. Spacecrafts modify them by their presence (wake, ram pressure increase) and above all by the emission of various products (see, e.g., the brief review in Ref. 1). The induced plasma environment can result in an electrically enhanced contamination, influence spacecraft charging, and enhance the risk of electrostatic discharges. Focus has recently been placed on the plasma environment created by electric propulsion devices, but this induced plasma always exists through ionization of neutrals by charge exchange (CEX) or ultraviolet (see Refs. 2, 3, or 4 or Ref. 5 for a review). A precise evaluation of this local environment and the damage it can induce requires a numerical simulation, and this is why the code for simulation of the local environment and contamination of spacecraft (SILECS), presented here, was created.

SILECS consists of a general framework for dealing with spacecraft geometry, preprocessing and postprocessing, and several modules describing different kinds of environments or physical phenomena. This paper describes the plasma environment module and the general framework. Other modules concerning the neutral environment, dust dynamics, and ejecta production by micrometeoroids are under development. All of the modules can communicate with one another: A neutral particle may be ionized and enter the plasma module, for instance, and the potential and densities computed by plasma and neutral modules are also used for the dust dynamics module, etc. This makes the tool quite powerful and innovative.

The model is described in the first section, and various methods of simulation are briefly discussed. The second section includes four SILECS simulation examples, essentially devoted to a validation of the code. The comparison to theoretical results was deliberately favored because it allows a more accurate testing of the model, whereas comparisons to experimental results always suffer from uncertainties due to the approximations of the physics involved. (A comparison of SILECS computations to experimental Langmuir probe characteristics can be found in Ref. 6.) This is why three simple cases, with known theoretical solutions, were selected as the first test cases of the second section. This allowed validation of the model over a range of situations. The fourth simulation of the second section demonstrates the potential applicability of the code to the more complex case of realistic spacecraft.

Received Jan. 10, 1997; revision received Oct. 17, 1997; accepted for publication Oct. 20, 1997.

*Research Scientist, Département d'Etudes et de Recherches en Technologie Spatiale, Centre d'Etudes et de Recherche de Toulouse.

Description of the Model

Introduction: Choice of the Method

Typical spatial densities, either of plasma or of neutrals, yield large mean free paths compared to spacecraft dimensions. Thermalization is, hence, very inefficient, and fluid equations such as Navier–Stokes equations are inadequate. Gases or plasmas (or even macroparticles) then must be described through their full distribution functions $f_s(\boldsymbol{x}, \boldsymbol{v}, t)$ in phase space. They obey the Boltzmann equation, or the Vlasov equation when collisions are neglected:

$$\frac{\mathrm{D}f_s}{\mathrm{D}t} = \frac{\partial f_s}{\partial t} + \boldsymbol{v} \cdot \frac{\partial f_s}{\partial \boldsymbol{x}} + \frac{q_s}{m_s}(\boldsymbol{E} + \boldsymbol{v} \times \boldsymbol{B})\frac{\partial f_s}{\partial \boldsymbol{v}} = \text{collision terms, or } 0 \tag{1}$$

The direct resolution of the Vlasov or Boltzmann equation in six-dimensional phase space is very costly in computer time and memory. This is why the Monte Carlo method was preferred, in particular, the direct simulation Monte Carlo method[7,8] (DSMC) for collisions of the Boltzmann equation. Beyond their somewhat more versatile character, Monte Carlo methods have the advantage of resulting in relatively faster codes, provided that some statistical noise is accepted because the reduction of numerical statistical fluctuations is again time consuming. From a mathematical point of view, this method gives approximate solutions of the Boltzmann equation, whereas from a physical point of view, it consists of sampling real particles and representing them by fewer numeric superparticles.

The dynamics of a plasma involving no electromagnetic wave activity is governed by the coupling of the Boltzmann and the Poisson equations. However, for charged particles, collisions are negligible with respect to electrostatic forces in usual applications. The model presented here is, therefore, a coupling of the Vlasov and the Poisson equations. This plasma module of the code is based on a code developed at the Département d'Etudes et de Recherches en Technologie Spatiale, which was devoted to steady-state computations of wakes on basic spacecraft geometries. (See the code description and comparison to experimental and in-flight results for a first two-dimensional code[9] and for a three-dimensional code.[10]) The evolution of the new plasma code is as follows: It computes real-time evolution owing to a true particle-in-cell (PIC) scheme (see subsection, "PIC Plasma Model"), which is more stable, deals with complex geometry (see next subsection, "Mesh"), and is integrated in the general frame, which makes it much more versatile (see subsection, "General Structure").

Mesh

In contrast with simpler methods such as ray tracing, as, e.g., in ESABASE,[11,12] or test particle Monte Carlo,[13] the Vlasov–Poisson equation resolution and the DSMC method require a three-dimensional mesh to compute local potential and autocoherent local densities.

A good approximation of the objects embedded in a computation box, concerning both surface position and orientation, is obtained by a triangulation of their surfaces. This creates an irregular two-dimensional mesh.[11,12,14] The natural three-dimensional continuation of this two-dimensional mesh is an unstructured mesh. However, unstructured meshes are not well suited for the Monte Carlo method because something as simple as determining in which cell a particle is becomes very time consuming. This drawback counterbalances the advantages of adaptability of unstructured meshes and makes the method hazardous, although possible. Another possibility is to simply embed objects in a structured mesh without any adaptation. A cell can then be only partially occupied by an object. It is possible to implement a DSMC code on such a mesh, but one must take special care of each cell that could be split by a thin surface so that particles of both sides do not collide (see, e.g., the SOCRATES code[15,16]). It seems, however, impossible to correctly solve the Poisson equation on such a mesh as one needs mesh points on object surfaces.

The chosen solution was to use a structured rectangular mesh with the capability of splitting cubes along face and cube diagonals. The possible geometry of objects is close to those of the NASCAP and POLAR codes.[17] However, the underlying method is very different. In the POLAR code, objects are built by hand from predefined building blocks, which are aggregates of (partial) cubes. On the contrary, here objects are defined from elementary geometrical shapes such as spheres, cones, prisms, plates, etc., which purely describe the geometry of spacecraft and have nothing to do with mesh. This object description language is hierarchical and compatible with ESABASE language.[11,12] The difficulty is then to embed these objects in a rectangular mesh allowing diagonally split cubes with the best approximation of surface position and orientation. A rather sophisticated algorithm that uses information concerning normals and edges of elementary shapes was implemented. Figure 1 shows two examples of elementary thin shapes giving the true normals (to a perfect cone or cylinder), approximated normals (to split cubes), and the angle between them. This angle is usually less than 25 deg (see the cylinder) but can sometimes be about 45 deg (see some surfaces of the cone). The true normals can be used for physical processes such as reflection and emission. (See, also, the subsequent wake simulation for normals and flux computation.) Other approximations of object surfaces can be seen in the geometry of the simulations described subsequently. The elementary shapes can be either volumes or surfaces, and different potentials can exist on both sides of surfaces.

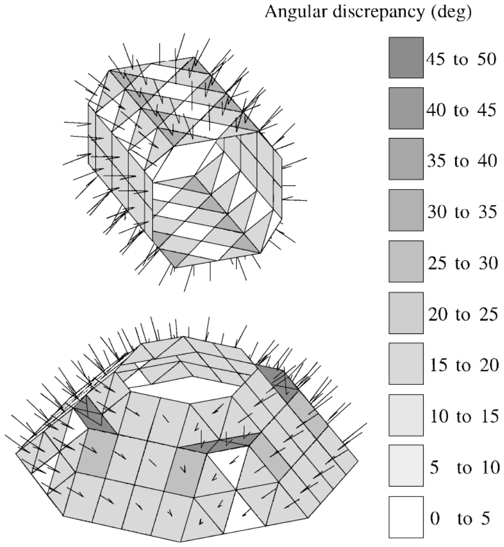

Fig. 1 Cylinder and cone with true and approximated normals to surfaces (long and short lines, respectively).

PIC Plasma Model

The Vlasov–Poisson equation is solved by a classical PIC method[18]: The particle dynamics in an electrostatic field (and possibly an external magnetic field) is modeled by the Monte Carlo method; each particle deposits its charge on the eight closest mesh points with volumic weight, which gives densities and allows the Poisson equation to be solved and then allows particle dynamics again to be computed.

The integration of particle trajectories is performed by a leapfrog method, exact to second order in time increment. The local electric field for a particle is obtained from the electric field at the eight closest mesh points through PIC volumic weights. This electric field at the mesh points is obtained from the potential at the six closest neighbors and does not need to be computed again for each particle. This and the use of volumic weights of the PIC method result in a rather fast algorithm. Moreover, it gives a continuous electrical field, which is exact to second order in the space interval.

For the time being, the Poisson equation is simply solved by the Gauss–Seidel iterative method. Implementation of a conjugate gradient method is foreseen but does not seem urgent because Poisson resolution is still shorter than particle motion in typical computations. The boundary conditions

$$E_n = -\chi_b / \alpha_{\mathrm{DN}} \tag{2}$$

can be of Dirichlet, Neumann, or mixed type for the α_{DN} length equal to ∞, 0, or in $]0, \infty[$, respectively. Mixed conditions are a way of simulating a potential that goes to zero at infinity but is not zero at boundaries. Potentials at the surface of objects may either be fixed or be left floating by capacitive coupling to a ground.

The electrons are usually supposed to be thermalized and described by a Boltzmann distribution. This is valid for negative potentials and in the absence of potential barriers. It gives a semilinear Poisson equation

$$-\Delta\,\chi(\boldsymbol{x}) = \left\{\rho_i(\boldsymbol{x}) - e\,n_0\exp\left[\frac{e\chi(\boldsymbol{x})}{kT_e}\right]\right\}\Big/\varepsilon_0 \qquad (3)$$

It is solved by an implicit Newton method.[19,20] However, the code is multispecies and the electrons can simply be modeled as one of the species, but this increases computation time dramatically because their dynamics necessitates much smaller time steps.

General Structure

All modules share the same common structure for geometry and graphical representations, as well as densities and fluxes, which allows intercommunicability. According to the general scheme, densities (respectively, fluxes) of charged or neutral particles are always represented by lists of superparticles inside the mesh (respectively, at the boundaries of mesh or objects). Thus, any kind of particle can experience (possibly reactive) collisions with another. Gas phase collisions can be performed either between lists of particles through DSMC (neutral module) or with a background density. The code structure allows modeling of any kind of elastic or reactive collision, e.g., CEX $\mathrm{Xe}^+ + \mathrm{Xe} \rightarrow \mathrm{Xe} + \mathrm{Xe}^+$, reaction $\mathrm{H_2O}^+ + \mathrm{H_2O} \rightarrow \mathrm{H_3O}^+ + \mathrm{OH}$, ionization, etc., but few cross sections are available yet. Collisions on surfaces can similarly be simulated for selected surface and particles, e.g., specified molecule and origin. The list of particles representative of the impinging flux is treated in a subroutine accounting for the physics involved (specular/accommodative bounce, neutralization of ions, sputtering, erosion by ATOX, etc.), which produces a list representative of the reemitted particles. An example of application to electric propulsion can be found in Ref. 21, where CEX in the plume, sputtering of solar arrays, and contamination by sputtering products were modeled. As another example, Langmuir probe characteristics in a ground facility containing fast ionospheric and slow CEX plasma were computed in Ref. 6 and allowed the determination of fast and slow plasma densities by comparison with experimental data.

The code was written in standard Fortran 90 and works on any UNIX workstation, although it was not primarily designed to be distributed to a large community. The inclusion of partial cubes into the mesh structure added some tests in the dynamics and Poisson equation resolution. These tests resulted in a more complex treatment of some particles and points close to partial cubes. It led to a longer code and lower optimization, increasing computation time by half. It takes now about 17 μs/particle/step for particle dynamics and 6 μs/cell/step for Gauss–Seidel Poisson on a basic DEC Alpha workstation or 10 μs/particle/step and 4 μs/cell/step on an SUN UltraSparc, respectively. The resulting global computation times range from tens of minutes to hours. Optimization is still in progress.

Examples of Simulations: Code Validation

Four simulations that primarily aim at testing the code accuracy and reliability are presented. Results of SILECS computations were compared with other results on simple plasma problems for which there exist either analytical results or specific reference models: one-dimensional Child–Langmuir law (first simulation) or Langmuir probes (second and third simulations). The last (fourth) simulation, which addresses the more complex case of a space station wake, the kind of problems the code is primarily devoted to, could be only partially validated.

Child–Langmuir Law (One Dimensional)

One of the simplest cases to test a plasma code is the one-dimensional Child–Langmuir law because the solution is analytical. This one-dimensional case was tested on the SILECS three-dimensional code by reducing two dimensions by translational invariance. Therefore, it amounted to testing a charge-limited collection of one charged species by a plane, with homogeneous injection of particles on the opposite boundary and periodic conditions for the other four boundaries.

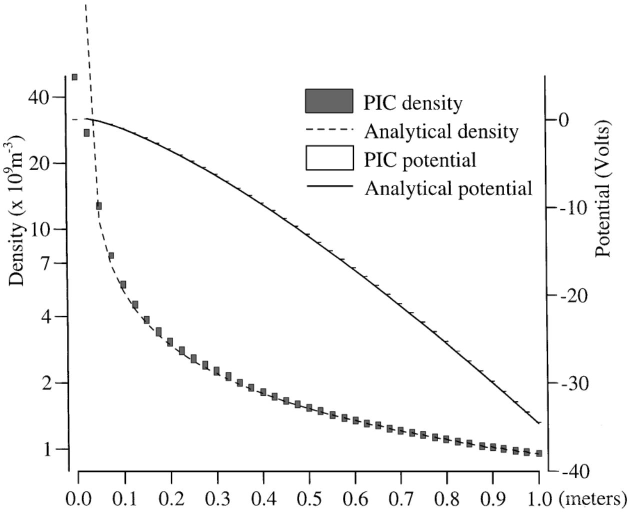

Fig. 2 Child–Langmuir law; comparison of PIC simulation and analytical results.

Figure 2 provides the density and potential vs distance to the injection plane. The bars are the simulation results. Their height gives the distribution dispersion to one standard deviation in the plane at the given distance. This dispersion is visible for density and negligible for potential. The lines show the analytical well-known results

$$\chi(x) = \chi_0\left(\frac{x}{L}\right)^{\frac{4}{3}}, \qquad n(x) = n_0\left(\frac{x}{L}\right)^{-\frac{2}{3}}, \quad \text{with} \quad n_0 = \frac{4\varepsilon_0|\chi_0|}{9eL^2} \qquad (4)$$

There are 40 cells in the relevant direction and 10 in the two others. Cells are cubic and 2.5 cm in size. The particles are positive ions of mass 18 ($\mathrm{H_2O}^+$), whereas experimentally electrons are more convenient. The agreement is very good, concerning both the space-dependent quantities of Fig. 2 and the total collected Child–Langmuir current density J_{CL} (see subsequent discussion).

In this simulation the only difficulty lies in the injection; the quantity of injected particles must be regulated by space charge. Therefore, more particles than necessary are injected, and the space charge builds up a small barrier of potential about 5 cm from the left-hand-side boundary of the computation box (too small to be visible in Fig. 2) that repels the particles of smallest energy. If the average energy, or temperature, of the injected particles is small, a small potential barrier is enough to repel all of them, which results in a very brutal and unstable autoregulation. Among injected particles of a higher temperature, however, only the slowest will be repelled by a small potential barrier, resulting in a smooth autoregulation. It must be realized that this regulation is nonlocal (the potential barrier comes from the space charge in the whole domain) and that its stability is, therefore, not as easy to achieve. However, the simulation becomes stable with a temperature of 1000 K (or 0.086 eV), which remains small compared to $\chi_0 = -35$ V, and so does not violate the assumption of zero-temperature particles of the Child–Langmuir law.

As a consequence of the potential barrier, the effective injection plane is shifted by 5 cm and the L parameter of the Child–Langmuir law is 0.95 m and not 1.00 m, the full size of the mesh. Thus, the analytical results yield the following values: $n_0 = 0.94 \times 10^9$ m^{-3} and $J_{\mathrm{CL}} = \sqrt{(2e/m_i)}4\varepsilon_0\chi_0^{3/2}/9L^2 = 2.9 \times 10^{-6}$ A/m^2, consistent with the numerical simulation results $n_0 = 0.95 \times 10^9$ m^{-3} [as shown in Fig. 2, giving $n(x)$] and $J_{\mathrm{CL}} = 3.0 \times 10^{-6}$ A/m^2. This also explains the difference between simulation and theory in the first 5 cm of Fig. 2: Theoretical density is infinite at 5 cm (injection plane) and undefined earlier, whereas PIC density gives the density at the left of the injection plane.

Spherical Langmuir Probe

The influence of the computation box size, cell size, boundary conditions, and time step was tested on the case of a spherical

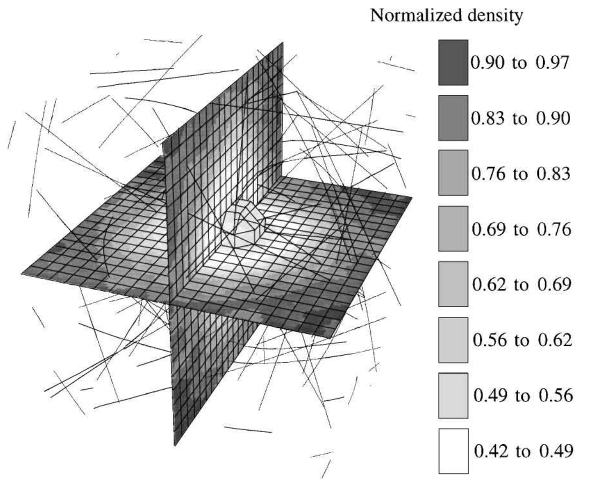

Fig. 3 Spherical Langmuir probe; cell size 5 mm, bias $-25kT_e/e$, density distribution and particle trajectories.

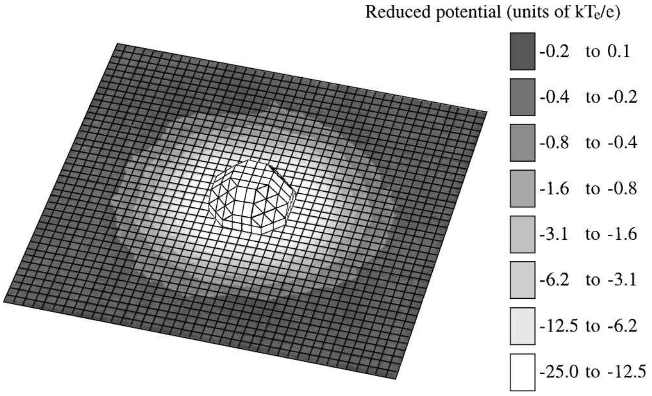

Fig. 4 Spherical Langmuir probe; cell size 2.5 mm, potential distribution.

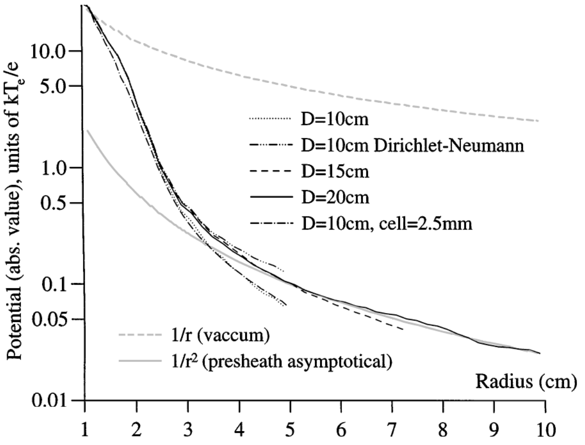

Fig. 5 Potential vs radius for various computation box sizes *D*.

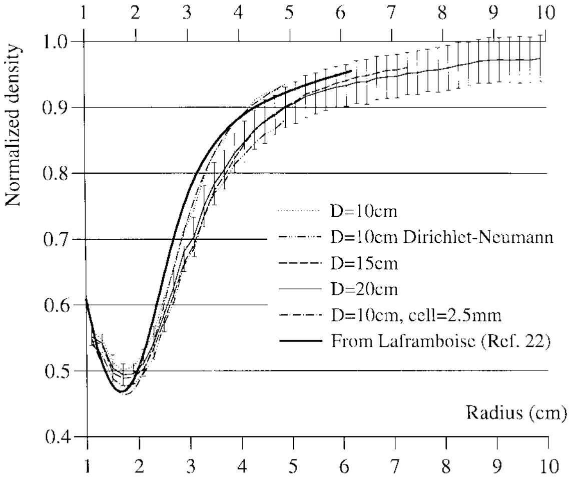

Fig. 6 Ion density vs radius for various computation box sizes *D*.

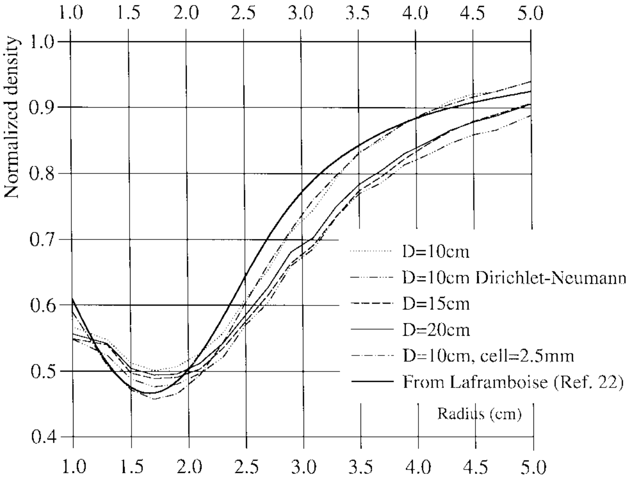

Fig. 7 Detailed ion density.

Langmuir probe. Most of these results could as well be compared with those obtained by Laframboise,[22] which can be considered as a reference concerning Langmuir probes.

A plasma at rest was modeled, with density 7×10^6 cm^{-3} for Ar$^+$ ions, ionic and electronic temperatures 0.5 eV or 5800 K, and, thus, of 2-mm Debye length. The probe radius was 1 cm. Two different cell sizes (5 and 2.5 mm), three different sizes of computation boxes (10, 15, and 20 cm), and two types of Dirichlet–Neumann boundary conditions were used. The integration time step for the particle trajectories was adjusted so that no particle crosses a cell in fewer than three steps. A shorter time step was attempted but did not significantly change the result and is not presented. It may slightly change individual trajectories due to improved numerical integration, but it did not affect the global densities and currents.

Figures 3 and 4 show the geometric approximation to a 1-cm-radius spherical probe for 5- and 2.5-mm cell sizes, respectively, and a computation box of 10 cm. As an example, particle trajectories, density, and potential are also shown on fictitious planes for a probe bias of -25 in electronic temperature units, i.e., -12.5 V.

For a more quantitative appreciation of potential and density, the profiles of all of the cases introduced before are given as a function of radius in Figs. 5 and 6 and in Fig. 7 as a zoom on the small-radius zone. The probe bias was held constant at $-25kT_e/e$. The standard boundary conditions are of Dirichlet type for the Poisson equation (potential fixed at zero), and the standard cell size is 5 mm. The nonstandard boundary condition and cell size are given in the legend for the two cases where they differ. The error bars in one of the density profiles of Fig. 6 give the density dispersion to one standard deviation. The errors are similar for other profiles and are not given for clarity's sake.

Potentials and densities from small-box simulations show some discrepancies with the ones from larger computation boxes (especially around the outside mesh boundaries). These discrepancies are small between 15- and 20-cm computation boxes, which indicates that a box of about 20 cm is sufficiently large. Not surprisingly, the discrepancies between 10- and 15-cm simulations are larger. It shows that, at a radius of 5 cm with a potential of about 0.1 kT_e/e, the presheath already begins: The approximate potential description in the 10-cm-box simulation with standard Dirichlet conditions ($\chi_b = 0$) yields too high a density. Therefore, better boundary conditions were tested, namely, mixed Dirichlet–Neumann conditions with $\alpha_{\mathrm{DN}} = r/2$ in Eq. (2), as proposed by Bernstein and Rabinowitz[23] from the asymptotical presheath potential in r^{-2} they computed for spherical probes. (This r^{-2} behavior in the presheath was checked in the 20-cm-box simulation, as shown in Fig. 5.) These

Table 1 Comparison between simulated and Laframboise[22] collected currents

	Real sphere	Simulation approximate sphere, cell = 2.5 mm	Simulation approximate sphere, cell = 5 mm
Surface, cm^2	12.6	15.1	16.2
Equivalent radius, cm	1.00	1.10	1.14
Radius /λ_{Debye}	5.0	5.5	5.7
Current of Ref. 22 Fig. 24 (normalized to thermal current density)	9.8	9.5	9.4
Current of Ref. 22, μA	6.0	7.0	7.5
Numerical simulation current, μA		6.7	7.6

boundary conditions give better agreement with larger-computation-box simulations.

The last simulation was performed with a cell size of 2.5 mm, standard Dirichlet conditions, and a 10-cm computation box (thicker line of Fig. 7). It exhibits differences with the corresponding 5-mm-cell simulation only at small radius. In the cases of coarser mesh (5-mm cells), the higher density value for radius between 1.4 and 2 cm, at the place of highest curvature, certainly comes from a smoothing of sharp variations due to lower spatial resolution. It is confirmed by the better agreement of finer-mesh results with those of Ref. 22 obtained with a specific model devoted to Langmuir probe simulations, as shown in Figs. 6 and 7 (thicker lines).

These thicker lines originate from the density profiles around a spherical probe for equal ionic and electronic temperatures given in Fig. 14 of Ref. 22 (for ratio of probe radius to Debye length of 5 in the present case). The general agreement with SILECS computations is good. It worsens in the small-radius zone, between 1.0 and 1.3 cm; the profile of Ref. 22 is convex and goes to 0.62 for radius 1.0 cm, whereas the profiles of Fig. 7 for cells of 5 mm have an inflection point and go only to 0.56. Here again better agreement is found for a finer mesh (2.5-mm-cell size), which shows no inflection point and goes to 0.59 of normalized density for minimal radius (Fig. 7). This proves that this slight discrepancy comes from the coarse mesh. The underestimated density at the probe surface was first thought to result from particles coming close to the probe at grazing incidence, which could be captured due to the rough approximation of a sphere used here (see Fig. 3), whereas they should not be captured by a perfect sphere. However, there are no such trajectories because it is not an orbital-motion-limited case[22] but a case of unpopulated (trapped) orbits. In fact, this discrepancy certainly also originates from the coarse mesh because there are few mesh points between 1.0 and 1.3 cm from probe center in the case of 0.5-cm cells.

The computed collected currents were finally compared with those of Ref. 22. In the case of 5-mm-cell simulations, the computed current shows little variation with computation box size or boundary conditions and remains between 7.45 and 7.70 μA. In the case of 2.5-mm cells, the current is 6.7 μA. The collected current is given in Fig. 24 of Ref. 22. It is 9.8 units of thermal current density, which is 49.1 nA/cm^2 for 5800-K Ar$^+$ ions. On a sphere of radius 1 cm it gives 6.0 μA, which is quite different from the present results. It turns out that the main cause of discrepancy is simply the size of the approximate spheres built from partial cubes: The spheres they approximate best are larger than 1 cm in radius. As shown in Table 1, equivalent radii were computed from the surfaces of the approximate spheres, and then new currents from Ref. 22 (7.0 and 7.5 μA) compare favorably with the values computed here.

Cylindrical Langmuir Probe

The bias of a cylindrical Langmuir probe was swept from 0 to −10 V or from 0 to $-50kT_e/e$ ($T_e = 0.2$ eV). The positive bias was not swept because electrons can no longer be described by a Boltzmann distribution, and simulating their dynamics would have led to very long simulations. To obtain a realistic time dependence, no underrelaxation was used. In this simulation, results again were compared to those of Ref. 22 (for permanent regime currents). This test case shows the real-time capabilities of the code, whereas all others were steady-state computations.

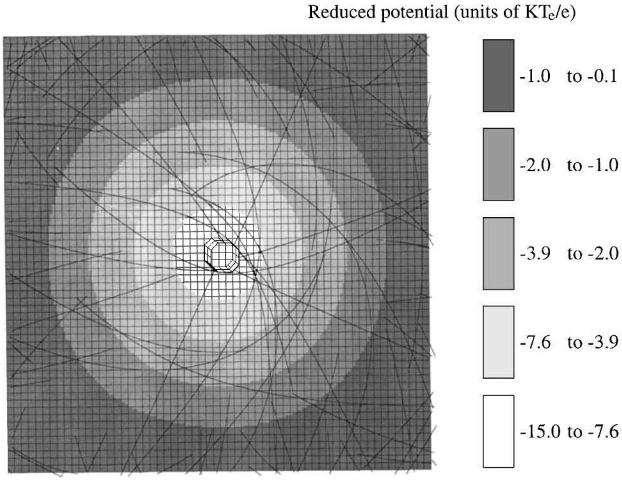

Fig. 8 Cylindrical Langmuir probe; potential and particle trajectories.

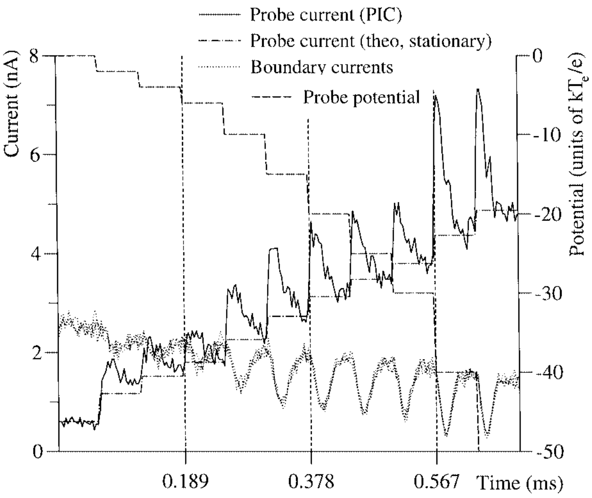

Fig. 9 Time evolution of currents and probe bias.

The mesh, the probe, and the potential distribution for the step −3 V are shown in Fig. 8. Some particle trajectories are also shown. Many of them appear to stop on the mesh boundary, but in fact they go on after symmetrization and are no longer shown. The three-dimensional mesh has been reduced to 2 cells of 5 mm in the invariant direction. There are 60 cells of 1 mm in the other two directions. The density of undisturbed Ar$^+$ plasma is 10^5 cm^{-3}. The ion and electron temperatures are both 0.2 eV. This results in a Debye length of 10 mm, much larger than the probe (and cell) size. Contrary to the last simulation (spherical probe with Debye length five times smaller than radius), this case is orbital-motion limited,[22] as can be checked on some particle trajectories approaching the probe at grazing incidence in Fig. 8 (as compared with Fig. 3).

Figure 9 shows the time variation of currents on the probe and on the mesh boundaries (except the two boundaries perpendicular to the probe axis). The potential bias of the probe is also included. At each new step of probe potential, the currents first exhibit a transient regime before they reach a permanent regime. It may be asked whether the permanent regime has really been reached at the end of each bias step of Fig. 9, inasmuch as the statistical fluctuations due to the rather small number of particles used for this simple test case make the asymptotical behavior of the curves not completely obvious. For some potential steps, it was checked on longer times that the permanent regime was effectively reached within the 0.063 ms of a step.

This transient regime is easy to understand; at each new step, the higher probe potential expands in the volume before the ions have enough time to react and to screen it by an enlarged sheath. More precisely, according to the method discussed earlier, intermediate time steps are used during which the ions move little but the electrons have time to thermalize. Numerically, this means that, between each step for ions, the semilinear Poisson equation (3) is solved, which includes the Boltzmann distribution of thermalized electrons. In fact, the electron density opposes the potential expansion but not the ion density as yet, and the potential expands more than it will in the permanent regime. This transiently too strong attractive potential results in transiently increased probe current and decreased boundary current. Note that this extension of potential up to the boundaries can make the results sensitive to the boundary conditions but only in the transient regime.

The current–voltage characteristics, obtained from asymptotic values of the permanent regime, are given in Fig. 10. The electron current is given by the thermal flux consistent with Boltzmann distribution

$$I_e = S\sqrt{kT_e/2\pi m_e}\,en_0\exp(e\chi/kT_e) \tag{5}$$

In this orbital-motion-limited case with large Debye length compared to probe radius, Laframboise[22] obtained an analytical expression for stationary ion current density [Eqs. (14.2) and (E.21) of Ref. 22], which can be written in dimensional form as

$$I_i = Sen_0\sqrt{\frac{kT_i}{2\pi m_i}}\frac{2}{\sqrt{\pi}}\left\{\sqrt{\frac{-e\chi}{kT_e}} + \frac{\sqrt{\pi}}{2}\left[1-\mathrm{erf}\left(\sqrt{\frac{-e\chi}{kT_e}}\right)\right]\right\} \tag{6}$$

with an undisturbed thermal ion current density $en_0(kT_i/2\pi m_i)^{1/2} = 0.443\ \mathrm{nA/cm^2}$. This ion current is given in Figs. 9 and 10 for all of the steps of χ. The PIC simulation current shows remarkable agreement with it. The electronic current of Ref. 22 is similar to the one used in Eq. (5) and is, therefore, not shown again.

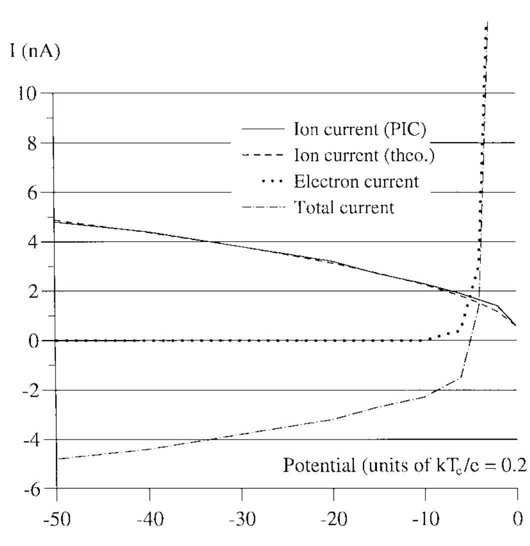

Fig. 10 I-V characteristics (built from Fig. 9).

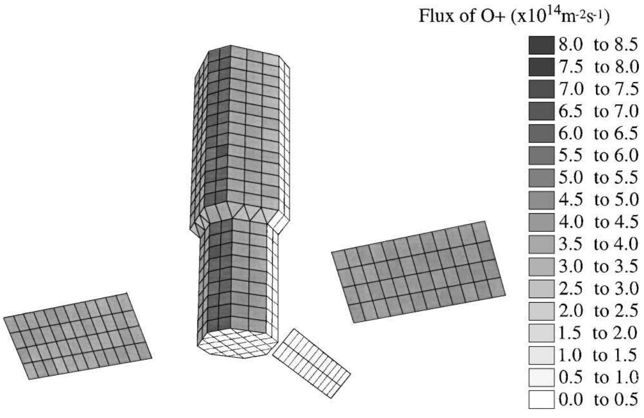

Fig. 11 Space station; view from ram, flux of oxygen ions.

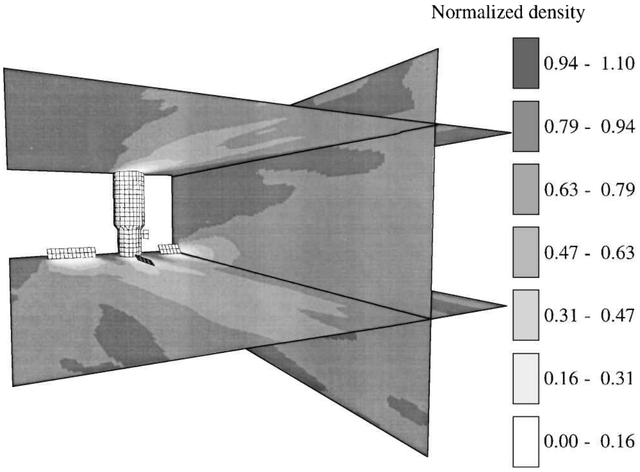

Fig. 12 Wake of a space station.

Complex Spacecraft Wake

The last simulation demonstrates the capability of SILECS to model complex realistic spacecraft. The wake structure of a small orbital station in low Earth orbit was computed. (It is composed, in fact, of the main modules of the MIR station, where the Echantillons module of the Aragatz experiment can be recognized.)

The mesh contains $40 \times 60 \times 80$ cubic cells of 60 cm. The plasma characteristics are typical of low Earth orbit: a density of $10^5\ \mathrm{cm}^{-3}$ for O^+ ions, an ionic temperature of 1000 K, an electronic temperature of 0.2 eV or 2320 K, and, hence, a Debye length of 1 cm, a drifting velocity of 7.8 km, and, with an acoustic ionic speed of 720 m/s, a Mach number of 11. The station geometry can be seen in Fig. 11, where the incident flux on ram surfaces was plotted. The flux variations intimately connected to the surface orientations reveal their imperfections. It is anticipated to improve the flux computation by taking into account the true normals to surfaces owing to a correction coefficient of the type $\cos(\theta)/\cos(\theta')$, with θ and θ' particle incidence angles with respect to the true and approximated normals, respectively. Figure 12 shows the plasma density on three fictitious planes, seen from wake side. The wakes of both solar panels and the main body combine.

The check that can be performed in this case concerns the potential in the first part of the wakes, where the ion density is zero. The lowest potential in the wakes (not represented here) is $-6.3kT_e/e$ behind solar panels, $-7.2kT_e/e$ behind the thinner part of the main body, and $-7.7kT_e/e$ behind the largest part of the main body. Theoretical values have been obtained for various geometries[24,25] and are all close to $-2\log(d/\lambda_{\mathrm{Debye}})$, where d is the object smallest dimension in the plane normal to speed. There are some extra constants depending on the considered geometry, which have a small contribution in the present case where $d/\lambda_{\mathrm{Debye}}$ is larger than 100. This gives theoretical potentials, respectively, of $-6.35kT_e/e$, $-7.17kT_e/e$ and $-7.74kT_e/e$, which are very close to ours, and even surprisingly close due to the approximate theoretical value. This essentially checks the resolution of the semilinear Poisson equation but not really the ion dynamics.

Discussion

The code validity was checked in several different cases. The first case, the one-dimensional Child–Langmuir law, showed good stability of the injection of one single-ion species (no electrons) and exhibited a very good agreement with the analytical solution. The next three cases were plasma simulations with a very wide range of cell size to Debye length ratios, 2.5, 0.1, and 60, respectively. In particular, the second and fourth simulations showed that the PIC scheme used (alternate resolution of dynamics and Poisson equation) is stable even for cells much larger than Debye length (60 times in the fourth case). Steady-states schemes, in which particles are moved all over the computation box before the Poisson equation is solved, are a priori not stable for such a large ratio.[26] Of course, structures at the level of Debye length cannot be modeled and are smoothed, e.g., wake boundaries in the last simulation, but the second simulation showed that this smoothing may not drastically affect variations at the scale of cell size.

The second simulation was certainly the most conclusive because detailed comparisons (density and potential profiles) were performed and the sensitivity to model parameters was examined. The various computation box sizes showed that the simulation was free of boundary effects for large-enough sizes and that mixed Dirichlet–Neumann boundary conditions could give better results for small sizes. Variation of cell size showed the limitations in the case of too coarse a mesh; too approximate an object description yields discrepancies at the object surface, and too large a cell size smooths sharp density variations (see Figs. 6 and 7). These drawbacks can be either accepted or corrected by using a finer mesh, as was done.

These examples also demonstrated some specific capabilities of the code. The third simulation showed a real-time computation, and the fourth one described a somewhat realistic and complex spacecraft geometry, although its capabilities are much larger, as was discussed in the preceding section.

Conclusions

A plasma model that constitutes one of the modules of the general code SILECS was presented. It will soon form an integrated simulation tool with the neutral environment, ejecta, and dust modules. The common geometrical frame has been devised to allow 1) the simulation of volume phenomena owing to a three-dimensional mesh (Poisson, Boltzmann equations), 2) the convenient use of Monte Carlo methods owing to a structured mesh, and 3) a correct description of spacecraft geometry owing to an automatic generation of split cubes from an object description language, and it seems to be a good compromise among these constraints.

The results of the four simulations described here were compared to established results. The comparisons were conclusive, exhibiting a good agreement most of the time and sometimes identifying the validity limits, usually due to coarse meshing. Now that the code has been tested to a large extent on pure cases, where the involved physical phenomena are identified, more complex in-flight or experimental realistic cases may be addressed, as exemplified by the case of the small station treated here, where the main issues are usually to correctly describe all of the relevant physical phenomena.

References

[1] Murad, E., "Spacecraft Interaction with Atmospheric Species in Low Earth Orbit," *Journal of Spacecraft and Rockets*, Vol. 33, No. 1, 1996, pp. 131–136.

[2] Caledonia, G. E., Person, J. C., and Hastings, D. E., "Ionization Phenomena About the Space Shuttle," U.S. Air Force Geophysics Lab., AFGL-TR-86-0045, Hanscom AFB, MA, Jan. 1986.

[3] Caledonia, G. E., Person, J. C., and Hastings, D. E., "The Interpretation of Space Shuttle Measurements of Ionic Species," *Journal of Geophysical Research*, Vol. 92, No. A1, 1987, pp. 273–281.

[4] Dressler, R. A., Gardner, J. A., Cooke, D. L., and Murad, E., "Analysis of Ion Densities in the Vicinity of Space Vehicles: Ion-Neutral Chemical Kinetics," *Journal of Geophysical Research*, Vol. 96, No. A8, 1991, pp. 13,795–13,806.

[5] Hastings, D. E., "A Review of Plasma Interactions with Spacecraft in Low Earth Orbit," *Journal of Geophysical Research*, Vol. 100, No. A8, 1995, pp. 14,457–14,483.

[6] Roussel, J.-F., Viel, V., and Bernard, J., "Characterization of a Multicomponent Plasma in an Ionospheric Plasma Simulation Chamber," *Proceedings of the International Conference on Phenomena in Ionized Gases*, Vol. 4, edited by M. C. Bordage, Université Paul Sabatier, Toulouse, France, 1997, pp. 130, 131.

[7] Bird, G. A., *Molecular Gas Dynamics*, Oxford Univ. Press, Oxford, England, UK, 1976, pp. 118–132.

[8] Bird, G. A., *Molecular Gas Dynamics and the Direct Simulation of Gas Flows*, 1st ed., Clarendon, Oxford, England, UK, 1994, pp. 148–182.

[9] Coggiola, E., and Soubeyran, A., "Mesothermal Plasma Flow Around a Negatively Wake Side Biased Cylinder," *Journal of Geophysical Research*, Vol. 96, No. A5, 1991, pp. 7613–7621.

[10] Maag, M.-C., "Modélisation Tridimensionnelle du Sillage d'un Satellite en Orbite Basse—Influence du Champ Magnétique Terrestre," Ph.D. Thesis, Centre d'Etudes et de Recherche de Toulouse–ONERA/Département d'Etudes et de Recherches en Technologie Spatiale, Ecole Nationale Supérieure de l'Aéronautique et de l'Espace, Toulouse, France, Dec. 1993.

[11] De Kruyf, J., "ESABASE: A Most Versatile and Flexible System engineering Tool," European Space Agency, ESA BR-54, European Space Research and Technology Center, Noordwijk, The Netherlands, Sept. 1988.

[12] Daly, E. J., Drolshagen, G., Tranquille, C., and De Kruyf, J., "Space Environment Analysis Tool," *Proceedings of the International Symposium on Environmental Testing for Space Programmes—Test Facilities & Methods*, European Space Agency, European Space Research and Technology Center, Noordwijk, The Netherlands, 1990, pp. 551–558.

[13] Fan, C., Gee, C., and Fong, M. C., "Monte Carlo Simulation for Backscatter of Outgassed Molecules from Simple Spacecraft Surfaces," *Journal of Spacecraft and Rockets*, Vol. 31, No. 4, 1994, pp. 649–654.

[14] Rault, D. F. G., and Woronowicz, M. S., "Application of Direct Simulation Monte Carlo to Satellite Contamination Studies," *Journal of Spacecraft and Rockets*, Vol. 32, No. 3, 1995, pp. 392–397.

[15] Elgin, J. B., and Sundberg, R. L., "Model Description for the SOCRATES Contamination Code," U.S. Air Force Geophysics Lab., AFGL-TR-88-0303, Hanscom AFB, MA, Oct. 1988.

[16] Elgin, J. B., Cooke, D. C., Tautz, M. F., and Murad, E., "Modeling of Atmospherically Induced Gas Phase Optical Contamination from Orbiting Spacecraft," *Journal of Geophysical Research*, Vol. 95, No. A8, 1990, pp. 12,197–12,208.

[17] Lilley, J. R., Jr., Cooke, D. L., Jongeward, G. A., and Katz, I., "POLAR User's Manual," U.S. Air Force Geophysics Lab., AFGL-TR-89-0307, Hanscom AFB, MA, Oct. 1989.

[18] Birdsall, C. K., and Bridges, W. B., *Plasma Physics via Computer Simulation*, McGraw–Hill, New York, 1985, pp. 19–22 and 311–315.

[19] Parker, L. W., "Calculation of Sheath and Wake Structure About a Pillbox-Shaped Spacecraft in a Flowing Plasma," *Proceedings of the Spacecraft Charging Technology Conference*, AFGL-TR-77-0051, NASA TMX-73537, 1977, pp. 331–366.

[20] Cooke, D. L., Katz, I., Mandell, M. J., Lilley, J. R. Jr., and Rubin, A. J., "Three-Dimensional Calculation of Shuttle Charging in Polar Orbit," N85-22486, U.S. Air Force Geophysics Lab., AFGL Contract F19628-82-C-0081, Hanscom AFB, MA, March 1985.

[21] Roussel, J.-F., Bernard, J., and Garnier, Y., "Numerical Simulation of Induced Environment, Sputtering and Contamination of Satellite due to Electric Propulsion," *Proceedings of the Second European Spacecraft Propulsion Conference*, European Space Agency, European Space Research and Technology Center, Noordwijk, The Netherlands, 1997, pp. 517–522.

[22] Laframboise, J. G., "Theory of Spherical and Cylindrical Langmuir Probes in a Collisionless, Maxwellian Plasma at Rest," Univ. of Toronto, UTIAS Rept. 100, Toronto, ON, Canada, June 1966.

[23] Bernstein, I. B., and Rabinowitz, I. N., "Theory of Electrostatic Probes in a Low Density Plasma," *Physics of Fluids*, Vol. 2, No. 2, 1959, pp. 112–121.

[24] Cooke, D. L., "Wake Effects in Spacecraft Charging," *Space Environment: Prevention of Risks Related to Spacecraft Charging*, Cépaduès, Toulouse, France, 1996, pp. 271–288.

[25] Crow, J. E., Auer, P. L., and Allen, J. E., "The Expansion of a Plasma into Vaccum," *Journal of Plasma Physics*, Vol. 14, Aug. 1975, pp. 65–76.

[26] Parker, L. W., and Sullivan, E. C., "Iterative Methods for Plasma-Sheath Calculations—Application to Spherical Probe," NASA TN D-7409, March 1974.

I. D. Boyd
Associate Editor